Adaptive multi-resolution 3D Hartree-Fock-Bogoliubov solver for nuclear structure

J. C. Pei (裴俊琛),[1,2,3] G. I. Fann,[4] R. J. Harrison,[5,6] W. Nazarewicz,[2,7,8] Yue Shi (石跃),[2,3] and S. Thornton[5]

[1]*State Key Laboratory of Nuclear Physics and Technology, School of Physics, Peking University, Beijing 100871, China*
[2]*Department of Physics and Astronomy, University of Tennessee, Knoxville, Tennessee 37996, USA*
[3]*Joint Institute for Nuclear Physics and Applications, Oak Ridge National Laboratory, Oak Ridge, Tennessee 37831, USA*
[4]*Computer Science and Mathematics Division, Oak Ridge National Laboratory, Oak Ridge, Tennessee 37831, USA*
[5]*Institute for Advanced Computational Science, Stony Brook University, Stony Brook, New York 11794, USA*
[6]*Computational Science Center, Brookhaven National Laboratory, Upton, New York 11973, USA*
[7]*Physics Division, Oak Ridge National Laboratory, Oak Ridge, Tennessee 37831, USA*
[8]*Institute of Theoretical Physics, Faculty of Physics, University of Warsaw, ul. Hoża 69, PL-00681 Warsaw, Poland*

Background: Complex many-body systems, such as triaxial and reflection-asymmetric nuclei, weakly bound halo states, cluster configurations, nuclear fragments produced in heavy-ion fusion reactions, cold Fermi gases, and pasta phases in neutron star crust, are all characterized by large sizes and complex topologies in which many geometrical symmetries characteristic of ground-state configurations are broken. A tool of choice to study such complex forms of matter is an adaptive multi-resolution wavelet analysis. This method has generated much excitement since it provides a common framework linking many diversified methodologies across different fields, including signal processing, data compression, harmonic analysis and operator theory, fractals, and quantum field theory.

Purpose: To describe complex superfluid many-fermion systems, we introduce an adaptive pseudospectral method for solving self-consistent equations of nuclear density functional theory in three dimensions, without symmetry restrictions.

Methods: The numerical method is based on the multi-resolution and computational harmonic analysis techniques with a multi-wavelet basis. The application of state-of-the-art parallel programming techniques include sophisticated object-oriented templates which parse the high-level code into distributed parallel tasks with a multi-thread task queue scheduler for each multi-core node. The internode communications are asynchronous. The algorithm is variational and is capable of solving coupled complex-geometric systems of equations adaptively, with functional and boundary constraints, in a finite spatial domain of very large size, limited by existing parallel computer memory. For smooth functions, user-defined finite precision is guaranteed.

Results: The new adaptive multi-resolution Hartree-Fock-Bogoliubov (HFB) solver MADNESS-HFB is benchmarked against a two-dimensional coordinate-space solver HFB-AX that is based on the *B*-spline technique and a three-dimensional solver HFODD that is based on the harmonic-oscillator basis expansion. Several examples are considered, including the self-consistent HFB problem for spin-polarized trapped cold fermions and the Skyrme-Hartree-Fock (+BCS) problem for triaxial deformed nuclei.

Conclusions: The new MADNESS-HFB framework has many attractive features when applied to nuclear and atomic problems involving many-particle superfluid systems. Of particular interest are weakly bound nuclear configurations close to particle drip lines, strongly elongated and dinuclear configurations such as those present in fission and heavy-ion fusion, and exotic pasta phases that appear in neutron star crust.

I. INTRODUCTION

The road map for nuclear structure theory includes QCD-derived (or inspired) nuclear interactions, *ab initio* calculations for light and medium nuclei, configuration-interaction approaches for near-magic systems, and density functional theory and its extensions for heavy, complex nuclei [1]. On the road to a quantitative understanding of nuclear structure and reactions, high-performance computing plays an increasingly important role. As stated in the recent decadal survey of nuclear physics [2], "high performance computing provides answers to questions that neither experiment nor analytic theory can address; hence, it becomes a third leg supporting the field of nuclear physics." The largest collaborations in computational nuclear structure and reactions involve nuclear theorists, computer scientists, and applied mathematicians to

break analytic, algorithmic, and computational barriers [1,3]. This paper offers an example of such a joint collaborative effort in the area of nuclear density functional theory (DFT).

A key element of any DFT framework is a HFB solver that computes self-consistent solutions of HFB (or Bogoliubov–de Gennes) equations. Traditionally, the HFB solvers in nuclear physics are based on the basis-expansion method, usually employing harmonic-oscillator wave functions [4–7]. These methods are very efficient but they require huge bases for cases involving weakly bound systems and large deformations [8,9]. On the other hand, solving HFB equations directly in coordinate space can offer very precise results [10–12]. Unfortunately, current HFB calculations for nonspherical geometries are computationally challenging. There exist two-dimensional (2D) coordinate-space HFB solvers based on *B*-splines which have provided precise descriptions of weakly bound nuclei and

large deformations [12,13]. However, the extension from 2D to fully three-dimensional (3D) HFB calculations adds at least three orders of computational complexities (for some recent developments, see Refs. [14–16]).

Similar to Fourier analysis, wavelet analysis deals with the expansion of functions in terms of basis functions. Unlike Fourier analysis, wavelet analysis expands functions not in terms of trigonometric functions but in terms of wavelets, which are generated by translations and dilations of a fixed function, called the mother wavelet. The wavelets obtained in this way have special scaling properties. They are localized in time and frequency, permitting more precise local connections between their coefficients and the function being represented. These estimates allow greater numerical stability in reconstruction and manipulation with controlled precision and sparsity. For example, the JPEG2000 compression algorithms were built by using wavelets. The decoding could be accomplished in multiple ways and enabled scalable compression with different resolution representations. By truncating the data stream early, a lower-resolution image is obtained.

Multi-wavelets consist of a set of wavelets. The Alpert multi-wavelets [17] that we use are constructed from Legendre polynomials. They are discontinuous and singular orthonormal functions which permit better approximation of singular and discontinuous functions with reduced Gibbs effects. Another feature is the availability of high vanishing moments, which permit the sparse representation and application of smooth functions and many singular operators in finite precision. Families of multi-wavelets permit high orders of approximations with fewer levels of refinement, which is essential for efficient scientific computing.

To this end, we have developed a 3D MADNESS-HFB solver for HFB equations and Hartree-Fock (HF) equations, which is a multi-resolution, adaptive spectral-approximation-based solver, by using a multi-wavelet basis with a scalable parallel implementation [18]. The new framework is applied to polarized ultracold Fermi gases in elongated optical traps as well as triaxial nuclei. In both cases, we will demonstrate the capability of very large box calculations which is essential for descriptions of complex geometries and topologies.

This paper is organized as follows: Section II briefly introduces the multi-resolution mathematics, low-separation-rank approximation, and parallel runtime environment. The iterative algorithm applied in MADNESS-HFB is presented in Sec. III. In Sec. IV, we benchmark MADNESS-HFB solutions for cold fermions and nuclei. Finally, conclusions are given in Sec. V.

II. MADNESS-HFB FRAMEWORK

Our implementation of MADNESS-HFB uses the Multi-resolution Adaptive Numerical Environment for Scientific Simulations (MADNESS) framework [18]. MADNESS is based on computational harmonic analysis and nonlinear approximations and uses Alpert's multi-wavelet basis [17,19,20] to represent functions. Fast parallel code development and scalable performance have been possible due to the ease of programming based on object-oriented abstractions for interprocessor communications, multi-threading, and mathematical operations.

A. Mathematics of MADNESS

The mathematics implemented in the MADNESS software are based on multi-resolution analysis (MRA) [19,20], nonlinear approximations, and pseudospectral techniques. There are two types of techniques used in MADNESS to approximate functions and operators. The first is the use of multi-resolution analysis based on Alpert's multi-wavelets [17]. The second technique is the use of the low-separation-rank approximations of Green's functions based on Gaussian functions [21,22]. In the following, we follow the notation and derivations of Ref. [20].

1. Multi-resolution analysis with wavelets

The application of MRA separates the behavior of functions and operators at different length scales in a systematic expansion. A consequence of the separation of scales is that each operator and wave function has a naturally independent adaptive refinement structure, reflected in terms of significant expansion coefficients of desired precision. The thresholding and truncation of expansion coefficients below a user-defined error provides adaptive blocks of nontrivial coefficients for a pseudospectral expansion. The union of the domains of the multi-wavelets with nonzero coefficients provide an adaptive dyadic spatial localization of the relevant contributions for the corresponding refinement levels. In one dimension (1D), the nonzero sets define an adaptive dyadic refinement and correspondingly in 3D a pruned octtree-type refinement.

The MRA representation used in MADNESS is analogous to that used in an adaptive hp-SEM (spectral element method), which employs elements of variable size h and piecewise-polynomial approximations of degree p. By suitably refining the mesh through h refinements (dividing the volume elements into smaller pieces) and p refinements (increasing the polynomial degree in the expansion within the elements), one can reach exponential convergence [23]. In MADNESS, for each function or operator, the union of the domains of the multi-wavelet basis functions with nonzero coefficients, after thresholding, defines an adaptive and hierarchical h structure and the associated multi-wavelets form the set of the piecewise polynomials up to order p. Thus, there are multiple $h - p$ refinement structures that are used simultaneously.

The basis of scaling functions in 1D is constructed in terms of the normalized Legendre polynomials rescaled to the unit interval $(0, 1)$ and zero elsewhere. For each level n (defining the volume refinement), the rescaled and translated basis function is given by

$$\phi_{il}^n(x) = 2^{n/2}\phi_i(2^n x - l), \qquad (1)$$

where $\phi_i(x) = \sqrt{2i + 1}P_i(2x - 1)$, with $P_i(x)$ being the Legendre polynomial on $(-1, 1)$, and is 0 elsewhere for $l = 0, \ldots, 2^n - 1$. The basis functions (1) at level n have domain of width 2^{-n}.

Let $V_n = \{\phi_{il}^n(x), i = 0, \ldots, k - 1\}$ be the span of the subspace at level n. Let $W_0 = \{\psi_i(x)\}$ denote an orthonormal basis which spans the difference subspace $V_1 - V_0$. These functions are called multi-wavelets. As with the scaling functions, let $\psi_{il}^n(x)$ and W_n denote the rescaled and shifted multi-wavelets and the corresponding subspace spanned by these functions at

level n. The definition of scaling functions and multi-wavelets defines an ascending sequence of subspaces

$$V_0 \subset V_1 \subset V_2 \cdots \subset V_n \qquad (2)$$

and

$$V_n = V_0 \oplus W_0 \oplus \cdots \oplus W_{n-1}, \qquad (3)$$

where $\oplus$ denotes the orthogonal sum. The dimension of V_i is greater than the dimension of the subspace V_{i-1}; thus, the basis functions of V_{i-1} and W_{i-1} can be written exactly in terms of the basis functions of V_i. These hierarchical linear algebraic relations between the bases defines the two-scale refinement structure between the coefficients at level $i-1$ and i and fundamentally defines the adaptive structure with a given threshold truncation.

A smooth function $f(x)$ in the subspace V_n can be approximated in terms of scaling functions as

$$f(x) = \sum_{l=0}^{2^n-1} \sum_{j=0}^{k-1} s_{jl}^n \phi_{jl}^n(x). \qquad (4)$$

Represented in the multi-wavelet basis, $f(x)$ is

$$f(x) = \sum_{j=0}^{k-1} s_j \phi_j(x) + \sum_{j=0}^{k-1} \sum_{m=1}^{n-1} \sum_{l=0}^{2^m-1} d_{jl}^m \psi_{jl}^m(x), \qquad (5)$$

with $s_{jl}^n = \int_{2^{-n}l}^{2^{-n}(l+1)} f(x)\phi_{jl}^n dx$ and $d_{jl}^m = \int_{2^{-m}l}^{2^{-m}(l+1)} f(x)\psi_{jl}^m dx$.

In the discussion above, we described the representations based on multi-wavelets in 1D. In 3D applications, we use tensor products of 1D multi-wavelets as well as scaling functions in nonstandard form. Figure 1 illustrates the multi-resolution structure of sample wave functions.

For smooth functions, the computational methodologies are guaranteed to approximate the solutions to the desired user precision ϵ, with respect to the relative norm, with the correct number of digits specified by the error. The estimate is based on truncating the difference coefficients in the multi-wavelet expansion,

$$||d_l^n||_2 = \sqrt{\sum_j |d_{jl}^n|^2} \leqslant \epsilon \min(1, 2^{-n}L), \qquad (6)$$

where L is the minimum of the width of the computational domain.

2. Multi-resolution

For the one-body Schrödinger equation,

$$(-\Delta + V)\psi = E\psi, \qquad (7)$$

the usual diagonalization approach is also derived and used. In this case, given a basis ψ_i, a Hamiltonian matrix is formed:

$$H_{i,j} = \langle \psi_i | -\Delta + V | \psi_j \rangle, \quad S_{i,j} = \langle \psi_i | \psi_j \rangle, \qquad (8)$$

to form a generalized eigenproblem $H\psi = S\psi$.

A generalized eigensolver computes the eigenvalues and the eigenvectors. The eigenvectors are coefficients with respect to the multi-wavelets basis, and they are converted back to the spectral representation for further computation. The Laplacian
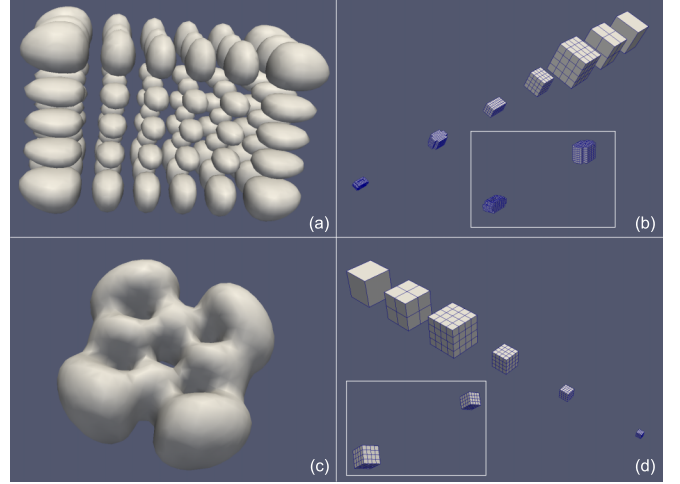

FIG. 1. (Color online) Pedagogical illustration of adaptive representations in MADNESS-HFB. (a) The modulus squared of the single-neutron wave function corresponding to the single-particle energy of -5.214 MeV obtained in MADNESS-HF calculations for ^{110}Mo (see Sec. IV B for details), and (b) the corresponding spectral refinement structure. (c) The modulus squared of the single-proton wave function corresponding to the energy eigenvalue -12.272 MeV in ^{110}Mo and its adaptive spectral structure in panel (d). Notice that the refinement structure for the proton wave function is similar to a truncated octtree-type of refinement but the structure for neutron wave function is more complicated, especially at the finer level [see insets in panels (b) and (d)].

Δ, the potential V, and the wave functions ψ_i are all in MRA form. The derivatives of multi-wavelets are expanded in terms of multi wavelets, and the coefficients are tabulated. By linearity, the derivatives of a function can be computed by matrix-vector products, or tensor-tensor products in higher dimensions, by using only the multi-wavelet coefficients.

This procedure permits computation of "self-consistent" solutions of DFT equations.

3. Low-separation-rank approximation of Green's functions

Recall that the (one-body) Schrödinger equation (7) can be rewritten as a Lippmann-Schwinger equation as

$$(\Delta + E)\psi = V\psi. \qquad (9)$$

There are several advantages of using the integral form (9) over the differential form (7). Namely, the integral form provides higher accuracy because high-frequency noise is attenuated instead of amplified, builds correct asymptotics, good condition number, and is potentially more computationally efficient. In most bases the Green's function representation is often dense, and the use of multi-resolution analysis and multi-wavelets provides fast algorithms with sparse structure in finite floating arithmetic with guaranteed precision. If no controlled truncations of the multi-wavelet coefficients are performed, the representation of the Green's function and its application will be dense.

The formal solution of Eq. (9) can be written as

$$\psi(r) = \int_{-\infty}^{\infty} G(r - r')V\psi(r')dr' = (G \star V\psi), \quad (10)$$

where the Green's function $G(r)$ is the Helmholtz kernel and the symbol $\star$ represents convolution. If the eigenvalue is bound ($E < 0$), the Green's function is the Yukawa potential $\exp(-kr)/r$ where $k = \sqrt{-E}$. In general, one works with $G = (\Delta + E + i\varepsilon)^{-1}$ with $\varepsilon \to +0$ and specifies how to integrate around the poles.

For bound states, a low-separation-rank (LSR) expansion [21,22] of the Yukawa potential is used:

$$\frac{e^{-kr}}{r} = \sum_l \sigma_l e^{-\tau_l r^2} + O(\epsilon). \quad (11)$$

The LSR approximation represents the Green's function in terms of a Gaussian expansion. Such a form reduces the application of 3D convolutions to an set of uncoupled 1D convolutions with the number of terms scaling logarithmically with respect to the relative precision ϵ. Since the convolution operator is linear, tables of precomputed transformation matrices with respect to the multi-wavelets enable fast applications of convolutions [24].

The technique described above to solve the Schrödinger equation can be directly applied to a HF problem, and—after a minor generalization—to HFB equations.

B. MADNESS parallel runtime environment

A novel parallel execution runtime environment has been implemented in the MADNESS software library. MADNESS uses one Message Passing Interface process to communicate between nodes, and POSIX threads within a node to exploit shared memory parallelism with a global addressable view of memory space in software. The MADNESS runtime is based on a parallel task-based computing model with a graph-based scheduler and a task queue on each node to enable distributed multi-threaded computation. A microparser is used to decouple tasks as much as possible but also to detect data dependencies so the most independent and out-of-order tasks can execute simultaneously, ensuring correct and minimal number of synchronization and thread termination.

Although the dedicated use of a core for internode communication and a core for handling thread scheduling may be a big sacrifice of computational resources, for supercomputers with large numbers of cores per node, we are able to obtain more than 50% of peak core performance for the remaining cores. Most scientific and engineering codes obtain only about 10% of the peak processor performance.

The flexibility of MADNESS-HFB in its design and programming style permits the solution of multiphysics problems with complex geometric structures and boundary conditions in large volumes in the coordinate-space formulation—limited only by the size of aggregate computer memory. Nuclear fission, exotic topologies in super- and hyperheavy nuclei, neutron star crusts, and cold atoms in elongated traps are some examples which can take advantage of these features.

III. MADNESS-HFB STRATEGY

The general HFB equation for a two-component (e.g., spin-up ↑ and spin-down ↓) system of fermions can be written as [25–28]

$$\begin{bmatrix} h_\uparrow - \lambda_\uparrow & \Delta \\ \Delta^* & -h_\downarrow + \lambda_\downarrow \end{bmatrix} \begin{bmatrix} u_i \\ v_i \end{bmatrix} = E_i \begin{bmatrix} u_i \\ v_i \end{bmatrix}, \quad (12)$$

where $h_\uparrow$ and $h_\downarrow$ are the Hartree-Fock Hamiltonians for the spin-up and spin-down components, respectively. The corresponding chemical potentials are denoted as $\lambda_\uparrow$ and $\lambda_\downarrow$, and the pairing potential is Δ.

There are two standard approaches to solve the HFB equation (12). In the basis-expansion method, eigenvectors (u_i, v_i) are expressed in terms of a single-particle basis and the self-consistent procedure applies the HFB Hamiltonian matrix diagonalization. The HFB solvers HFBTHO [4] (using the cylindrical transformed deformed harmonic-oscillator basis) and HFODD [7] (using the Cartesian deformed harmonic-oscillator basis), employed in this work to benchmark MADNESS-HFB belong to this class. A second way is to solve the HFB equations in the coordinate space by finite-difference or finite-element methods [12,13,29] or in momentum space by using fast Fourier transforms [30]. The strategy applied in MADNESS-HFB, described in Sec. II, combines features from these two approaches. The original method was developed in the context of HF and DFT problems in computational chemistry [22,31].

To illustrate the self-consistent procedure, let us consider a case of an unpolarized system ($h_\uparrow = h_\downarrow$) with constant effective mass $1/\alpha$. The mean-field Hamiltonian is

$$h(\mathbf{r}) = -\frac{\alpha \nabla^2}{2} + U(\mathbf{r}), \quad (13)$$

where $U(\mathbf{r})$ is the HF potential. As discussed in Sec. II A 3, it is convenient to rewrite the HFB equation (12) in a Lippmann-Schwinger form. To this end, in each step of HFB iteration, we introduce the Green's functions G_+ and G_-:

$$G_\pm^n = \frac{1}{\frac{\alpha\nabla^2}{2} + (E_s \pm E_i^n)}, \quad (14)$$

where E_i^n is the ith HFB eigenvalue in the nth iteration step, and E_s is the energy displacement that shifts the positive-energy HFB eigenvalues so that the associated Green's function is properly defined.

To solve the self-consistent HFB eigenproblem, the HFB wave functions can be updated as follows:

$$u_i^{n+1} = \left(G_+^n \star \left[(U - \lambda)u_i^n + \Delta v_i^n + E_s u_i^n\right]\right), \quad (15a)$$

$$v_i^{n+1} = \left(G_-^n \star \left[(U - \lambda)v_i^n - \Delta u_i^n + E_s v_i^n\right]\right). \quad (15b)$$

Following this strategy, in the following section, we use MADNESS-HFB to solve HFB problems with advanced local energy density functionals for cold fermions and nuclei.

IV. BENCHMARK PROBLEMS

In this section, the MADNESS-HFB framework is benchmarked by solving HFB equations for a trapped unitary

Fermi gas and HF-BCS equations for a triaxial nucleus. The MADNESS-HFB solutions for atoms and nuclei are compared with results of 2D HFB-AX and 3D HFODD calculations, respectively.

A. HFB solver for unitary Fermi gas

The unitary limit of a Fermi gas is characterized by an infinite s-wave scattering length. Of particular interest are superfluid phases in spin-imbalanced systems, such as the Fulde-Ferrell-Larkin-Ovchinnikov [32,33] phase that exhibits oscillating pairing gaps. The ultracold fermions at the unitary limit can be described by the superfluid density functional SLDA [34] and its asymmetric extension ASLDA for spin-polarized systems [25].

The single-particle Hamiltonian of the ASLDA for asymmetric systems can be written as [25]

$$h_\sigma = -\frac{\hbar^2}{2m}\nabla \cdot [\nabla \alpha_\sigma(\mathbf{r})] + U_\sigma(\mathbf{r}) + V_{\text{ext}}(\mathbf{r}), \quad (16)$$

where $\sigma = (\uparrow, \downarrow)$ denotes the spin-up and spin-down components. The local polarization is denoted as $x(\mathbf{r}) = \rho_\downarrow(\mathbf{r})/\rho_\uparrow(\mathbf{r})$ with $x(\mathbf{r}) \leq 1$, where $\rho_\uparrow(\mathbf{r})$ and $\rho_\downarrow(\mathbf{r})$ are densities of spin-up and spin-down atoms, respectively. The total polarization of the system is $P = (N_\uparrow - N_\downarrow)/N$. The quantity $\alpha_\sigma(x(\mathbf{r}))$ is the local effective mass. The SLDA formalism can be obtained from ASLDA by assuming $x(\mathbf{r}) = 1$, resulting in identical effective masses and Hartree potentials for spin-up and spin-down species.

The cold atoms are trapped in an external potential

$$V_{\text{ext}}(x, y, z) = V_0 \left\{ 1 - \exp\left[-\frac{\omega^2(x^2 + y^2 + z^2/\eta^2)}{2V_0} \right] \right\}, \quad (17)$$

where the trap aspect ratio η denotes the elongation of the optical trap potential. The equations are normalized so that $\hbar = m = \omega = 1$ (trap units). All other details pertaining to our SLDA and ASLDA calculations closely follow Ref. [28].

We first consider an SLDA case of ten particles in a spherical trap with $V_0 = 10$ and the quasiparticle energy cutoff $E_{\text{cut}} = 6$. The calculations were performed in a 3D box $(-L, L)^3$ with $L = 60$ With this box and cutoff, the self-consistent HFB solution involves 296 one-quasiparticle eigenfunctions. In the present SLDA and ASLDA benchmark calculations, we adopt wavelet order of $p = 8$ with a requested truncation precision of $\epsilon = 10^{-5}$ (see Eq. (6)).

The MADNESS-HFB results were benchmarked by using the 2D HFB solver HFB-AX. In the HFB-AX calculation, the maximum mesh size is 0.3, the order of B-splines is $k = 12$, and the box size is $R_{\text{max}} = Z_{\text{max}} = 14$. The eigenvalues and occupation numbers of some of the lowest and highest states from the two codes are compared in Table I. The agreement is excellent, also for the total energy and chemical potential.

Next we consider the functional ASLDA, which was developed to describe polarized Fermi systems. Because of nonzero spin polarization, the corresponding HFB solutions break time-reversal symmetry. In the first test, we performed MADNESS-HFB and HFB-AX simulations for 10 particles with a total polarization of $P = 0.1$ in a spherical trap. As seen in

TABLE I. Benchmark comparison of MADNESS-HFB and HFB-AX results for 10 particles in the spherical trap without polarization. Displayed are one-quasiparticle energies E_i, occupations v_i^2, chemical potential λ, and total energy E_t. Each one-quasiparticle state is labeled by means of orbital quantum number ℓ and parity $\pi = (-1)^\ell$. Note that every solution is $(2\ell + 1)$-folded degenerate with respect to the magnetic quantum number. The numbers in parentheses denote powers of 10. The energy is expressed in trap units ($\hbar = m = \omega = 1$).

		MADNESS-HFB		HFB-AX	
i	ℓ	E_i	v_i^2	E_i	v_i^2
1	0	0.90394	0.23240	0.90395	0.23240
2	2	1.06340	0.17779	1.06342	0.17779
3	1	1.12686	0.47471	1.12688	0.47469
4	3	1.92205	2.2491(−2)	1.92206	2.2491(−2)
5	1	2.00891	0.28448	2.00894	0.28449
6	0	2.54095	0.30390	2.54096	0.30393
7	2	2.69803	3.3837(−2)	2.69804	3.3838(−2)
8	0	2.82496	0.60883	2.82500	0.60884
9	4	2.91835	3.8699(−3)	2.91836	3.8698(−3)
10	1	3.44774	2.3162(−2)	3.44775	2.3165(−2)
21	7	5.54071	3.1957(−5)	5.54072	3.1954(−5)
22	2	5.58728	3.6548(−3)	5.58728	3.6550(−3)
23	4	5.75254	1.8024(−3)	5.75255	1.8024(−3)
		$E_t = 18.5641$		$E_t = 18.5639$	
		$\lambda = 2.24917$		$\lambda = 2.24916$	

Fig. 2, the density distributions for the spin-up and spin-down components agree very well between MADNESS-HFB and HFB-AX. Some of the eigenvalues are compared in Table II. Note that the calculation conditions adopted in Tables I and II are the same. It can been seen that the agreement is good up to the fourth digit since the calculations of local polarization $x(\mathbf{r}) = \rho_\downarrow(\mathbf{r})/\rho_\uparrow(\mathbf{r})$ may lose accuracy in both approaches when both the spin-up and spin-down densities are very small. In this case, required precision ALSDA should be significantly greater than that requested in SLDA calculations.
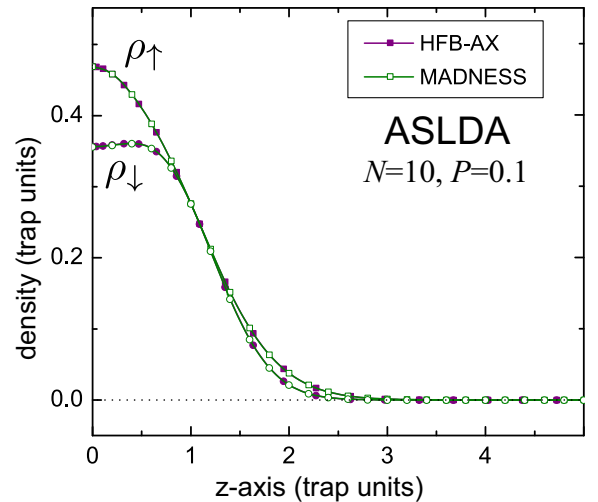

FIG. 2. (Color online) Comparison between density distributions $\rho_\downarrow(\mathbf{r})$ and $\rho_\uparrow(\mathbf{r})$ obtained in ASLDA with MADNESS-HFB and HFB-AX for 10 particles in a spherical trap with polarization $P = 0.1$.

TABLE II. Similar to Table I but for a polarized system in ASLDA.

i	MADNESS-HFB		HFB-AX	
	E_i	v_i^2	E_i	v_i^2
1	−0.1333	0.2090	−0.133**0**	0.209**1**
2	0.0463	0.1493	0.046**8**	0.149**4**
3	0.0786	0.4684	0.078**7**	0.468**2**
4	0.8837	0.1740(−1)	0.883**8**	0.174**2**(−1)
5	1.0157	0.2749	1.016**1**	0.275**0**
6	1.5425	0.2931	1.5425	0.292**7**
7	1.6944	0.3221(−1)	1.694**3**	0.322**5**(−1)
8	1.8346	0.6160	1.834**8**	0.616**1**
23	4.6417	0.0155(−1)	4.641**6**	0.015**6**(−1)
24	4.8158	0.1689(−5)	4.815**7**	0.169**2**(−5)
	$E_t = 19.0436$		$E_t = 19.044$**3**	
	$(\lambda_\uparrow + \lambda_\downarrow)/2 = 2.1684$		$(\lambda_\uparrow + \lambda_\downarrow)/2 = 2.168$**3**	
	$N_\uparrow - N_\downarrow = 1.0034$		$N_\uparrow - N_\downarrow = 1.003$**38**	

To demonstrate the capability of MADNESS-HFB for accurate simulation of large systems, we carried out SLDA simulations for 100 particles with polarization $P = 0.2$ in an elongated trap with $\eta = 16$. The choice of SLDA was motivated by the above-mentioned loss accuracy of ASLDA caused by a numerical error on $x(\mathbf{r})$ at low densities (large distances). The simulation box is $(-L, L)^3$ with $L = 120$. This computation involves about 2000 eigenstates and 5000 cores on the Titan supercomputer, and takes about four hours to reach convergence. The total and polarization densities for the MADNESS-HFB and HFB-AX simulations are shown in Fig. 3. The 3D pairing potential is displayed in Fig. 4. The oscillations of the pairing field in a spin-polarized system, characteristic of the Larkin-Ovchinnikov phase, are clearly seen (see Ref. [28] for more discussion).

B. Skyrme HF + BCS solver for nuclei

Most of the currently envisioned applications of MADNESS-HFB pertain to the nuclear many-body problem. To this end, the
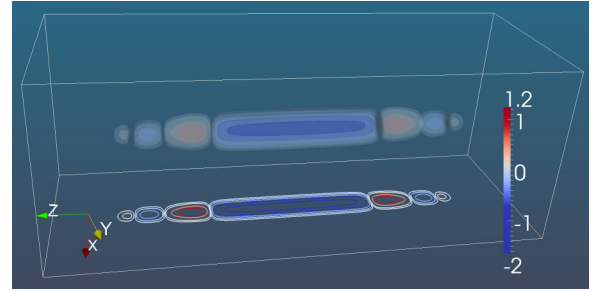
FIG. 4. (Color online) The pairing potential of 100 particles with $P = 0.2$ in an elongated trap with $\eta = 16$ computed with SLDA.

adaptive multi-resolution Skyrme-HFB solver has also been developed. The MADNESS-HFB approach for nuclei is similar to the SLDA for cold atoms but much more involved due to the continuum discretization, because the atomic nucleus is an open system and associated boxes are large [35]. Therefore, as an initial step, we carry out Skyrme HF and Skyrme HF + BCS calculations and benchmark them with HFODD.

For both HF and HF + BCS calculations, we consider the neutron-rich nucleus ^{110}Mo which is triaxially deformed in its ground state in some models [36]. We use SkM* [37] Skyrme parametrization, and take $\hbar^2/(2m) = 20.73$ MeV fm^2 for benchmarking purposes.

In pairing calculations for ^{110}Mo, due to the small neutron separation energy, the positive-energy HF levels are important because they participate in pairing. This creates a problem when trying to compare BCS or HFB results based on solvers that use a coordinate-space framework and a harmonic-oscillator expansion because the continuum representation is different in both approaches. Indeed, coordinate-space solvers MADNESS-HF or MADNESS-HF+BCS, when applied to large boxes, produce a very dense unbound single-neutron spectrum [11,35,38]. On the other hand, the single-neutron spectrum of oscillator-based HFODD is fairly sparse. Therefore, to minimize the difference between these two codes for a meaningful benchmarking, we switch off neutron pairing and retain only bound 70 single-proton orbits in the BCS phase space. We adopt a mixed density-dependent delta interaction [39]. The proton pairing strength is chosen to be −500 MeV to obtain a paired solution. Our MADNESS-HF and MADNESS-HF+BCS calculations are performed in a large 3D box $(-L, L)^3$ with $L = 50$ fm. The wavelet order is $p = 9$ with requested truncation precision $\epsilon = 10^{-7}$. HFODD calculations are performed with 1140 and 1540 spherical harmonic oscillator states, corresponding to 17 and 19 shells, respectively. The oscillator constant is 0.497 589 0 fm^{-1}. In MADNESS, the Coulomb potential can be obtained very effectively by using the separated form of the Poisson kernel [22].

Since MADNESS calculations are numerically extensive, it is desirable to warm start the runs with wave functions (or densities) from the converged HFODD solution. We have implemented such an interface between HFODD and MADNESS-HFB.

Table III compares MADNESS-HF and HFODD results for the triaxial ground-state configuration in ^{110}Mo.
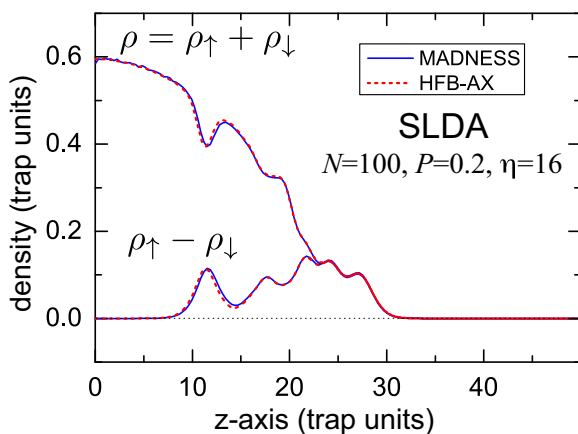

FIG. 3. (Color online) Comparison between density distributions $\rho_\uparrow + \rho_\downarrow$ and $\rho_\uparrow - \rho_\downarrow$ obtained in SLDA with MADNESS-HFB and HFB-AX for 100 particles with $P = 0.2$ in an elongated trap with $\eta = 16$.

TABLE III. Comparison between results of MADNESS-HF and HFODD for the triaxial ground state of ^{110}Mo: total binding energy E_t, kinetic energy E_{kin}, Coulomb energy E_c, and spin-orbit energy E_{SO} (all in MeV), mass r.m.s. radius R_{rms} (in fm), and mass quadrupole moments Q_{20} and Q_{22} (in fm^2). The "0th iter" column shows MADNESS-HF warm-start numbers at the beginning of the iteration process with wave functions and densities imported from converged HFODD results using 1140 basis states.

	HFODD (1140)	HFODD (1540)	MADNESS-HF (0th iter)	MADNESS-HF (converged)
E_t	−921.803	−921.932	−921.808	−922.119
E_{kin}	1998.074	1998.316	1998.075	1998.846
E_c	251.116	251.128	251.116	251.138
E_{SO}	−69.290	−69.273	−69.290	−69.276
R_{rms}	4.6696	4.6697	4.6696	4.6697
Q_{20}	914.12	913.58	914.12	913.69
$|Q_{22}|$	367.93	368.48	367.93	368.88

The MADNESS-HF results labeled "0th iter" are warm-start initialization numbers, with densities imported from HFODD(1140). As expected, "0th iter" and HFODD (1140) values are extremely close. A very small difference ≈ 5 eV on the total energy can be attributed to the potential (Skyrme) energy. In particular, the density-dependent term ($\sim \rho^{\gamma+2}$) produces the largest difference. The excellent agreement between these two calculations indicates that the interface between the two solvers has been implemented correctly, and that the individual Skyrme EDF terms have been coded properly in MADNESS-HF. By increasing the basis size in HFODD to 1540 states, the total binding energy decreases by ~ 130 keV. However, it is still ~ 190 keV above the MADNESS-HF result. This difference can be traced back to asymptotic behavior of nucleonic densities obtained in the two solvers. Figure 5 displays the neutron density profiles along the x-, y-, and z-axes (moving from the origin) computed in HFODD (1140), HFODD (1540), and MADNESS-HF. When displayed on a linear scale, one can hardly see a difference between HFODD and MADNESS-HF predictions. However, when inspecting the density in a logarithmic scale, one can see a characteristic damping at large distances (10–12 fm) in HFODD due to the finite size of oscillator basis. We recall that the MADNESS-HF calculations were carried out in a box extending to 50 fm. It is worth noting that, in a 2D (axial) case, similar conclusions have been reached when comparing coordinate-space and HO-basis HFB solvers [12,40].

Finally, Table IV displays HF + BCS results. Again, the agreement between MADNESS-HFB and HFODD is excellent, with the total binding energy in MADNESS-HFB being ~ 150 keV below that of HFODD (1540).

V. SUMMARY

In this paper, we introduce nuclear DFT framework based on the adaptive multi-resolution 3D HFB solver MADNESS-HFB. The numerical method employs harmonic analysis techniques with a multi-wavelet basis; user-defined finite precision is guaranteed. The solver applies state of the art
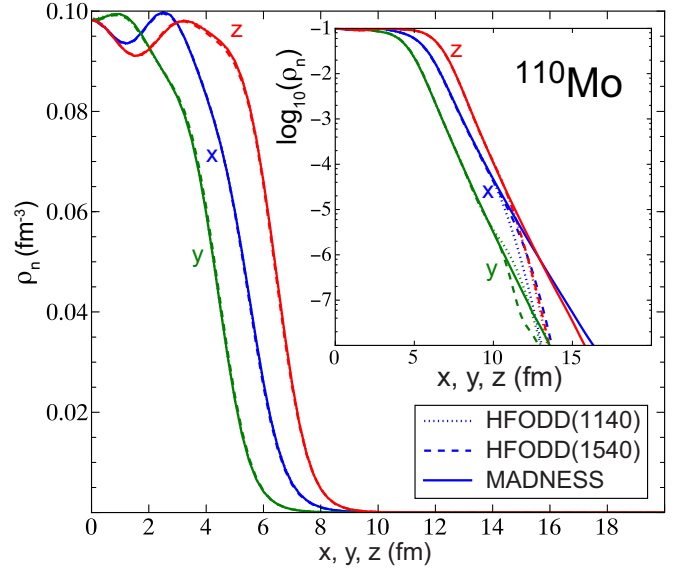

FIG. 5. (Color online) Neutron density distribution for ^{110}Mo in MADNESS-HF (solid line), HFODD (1140) (dotted line), and HFODD (1540) (dashed line) along the x-, y-, and z-axes, moving from the origin. The inset (in a logarithmic scale) illustrates the tail behavior of density.

in parallel programming techniques that can take advantage of high-performance supercomputers.

Applications have been presented for polarized ultracold atoms in very elongated traps and for triaxial neutron-rich nuclei. The solver has been benchmarked against other advanced HFB solvers: a 2D coordinate-space solver HFB-AX based on the B-spline technique and a 3D solver HFODD employing the harmonic-oscillator basis expansion. The advantage of MADNESS-HFB is its ability to treat large and complex systems without restriction on symmetries. Examples of future nuclear structure applications include weakly bound nuclei with large spatial extensions, heavy-ion fusion, nuclear fission, complex topologies in super- and hyperheavy nuclei [41–43], and pasta phases in the inner crust of neutron stars [44–47]. Future atomic applications of MADNESS-HFB include the description of a large number of fermions ($\sim 10^5$) in highly elongated optical traps ($\eta \sim 50$) [48].

TABLE IV. Similar to Table III, except that we include BCS pairing for protons. See text for details.

	HFODD (1140)	HFODD (1540)	MADNESS-HF (0th iter)	MADNESS-HF (converged)
E_t	−922.419	−922.549	−922.425	−922.707
E_{pair}	−4.981	−4.988	−4.981	−4.781
λ_p	−12.688	−12.692	−12.688	−12.697
E_{kin}	1998.055	1998.285	1998.055	1998.607
E_c	251.239	251.252	251.239	251.250
E_{SO}	−67.251	−67.228	−67.251	−67.220
R_{rms}	4.6610	4.6611	4.6610	4.6615
Q_{20}	859.64	858.74	859.64	860.91
$|Q_{22}|$	355.92	356.58	355.92	357.91

[1] S. Bogner *et al.*, Comput. Phys. Commun. **184**, 2235 (2013).

[2] *Nuclear Physics: Exploring the Heart of Matter. Report of the Committee on the Assessment of and Outlook for Nuclear Physics* (The National Academies Press, Washington, DC, 2013).

[3] G. F. Bertsch, D. J. Dean, and W. Nazarewicz, SciDAC Rev. **6**, 42 (2007).

[4] M. Stoitsov, J. Dobaczewski, W. Nazarewicz, and P. Ring, Comput. Phys. Commun. **167**, 43 (2005).

[5] M. V. Stoitsov, N. Schunck, M. Kortelainen, N. Michel, H. Nam, E. Olsen, J. Sarich, and S. Wild, Comput. Phys. Commun. **184**, 1592 (2013).

[6] J. Dobaczewski and P. Olbratowski, Comput. Phys. Commun. **158**, 158 (2004).

[7] N. Schunck, J. Dobaczewski, J. McDonnell, W. Satuła, J. Sheikh, A. Staszczak, M. Stoitsov, and P. Toivanen, Comput. Phys. Commun. **183**, 166 (2012).

[8] N. Michel, K. Matsuyanagi, and M. Stoitsov, Phys. Rev. C **78**, 044319 (2008).

[9] M. Kortelainen, J. McDonnell, W. Nazarewicz, P.-G. Reinhard, J. Sarich, N. Schunck, M. V. Stoitsov, and S. M. Wild, Phys. Rev. C **85**, 024304 (2012).

[10] J. Dobaczewski, H. Flocard, and J. Treiner, Nucl. Phys. A **422**, 103 (1984).

[11] J. Dobaczewski, W. Nazarewicz, T. R. Werner, J. F. Berger, C. R. Chinn, and J. Dechargé, Phys. Rev. C **53**, 2809 (1996).

[12] J. C. Pei, M. V. Stoitsov, G. I. Fann, W. Nazarewicz, N. Schunck, and F. R. Xu, Phys. Rev. C **78**, 064306 (2008).

[13] E. Terán, V. E. Oberacker, and A. S. Umar, Phys. Rev. C **67**, 064314 (2003).

[14] I. Stetcu, A. Bulgac, P. Magierski, and K. J. Roche, Phys. Rev. C **84**, 051309 (2011).

[15] Y. Hashimoto, Phys. Rev. C **88**, 034307 (2013).

[16] A. Bulgac and M. M. Forbes, Phys. Rev. C **87**, 051301 (2013).

[17] B. Alpert, SIAM J. Math. Anal. **24**, 264 (1993).

[18] MADNESS website http://code.google.com/p/m-a-d-n-e-s-s/.

[19] S. G. Mallat, Trans. Am. Math. Soc. **315**, 69 (1989).

[20] B. Alpert, G. Beylkin, D. Gines, and L. Vozovoi, J. Comput. Phys. **182**, 149 (2002).

[21] G. Beylkin and M. J. Mohlenkamp, Proc. Natl. Acad. Sci. USA **99**, 10246 (2002).

[22] R. J. Harrison, G. I. Fann, T. Yanai, Z. Gan, and G. Beylkin, J. Chem. Phys. **121**, 11587 (2004).

[23] I. Babuška and B. Q. Guo, Adv. Eng. Soft. **15**, 159 (1992).

[24] G. I. Fann, R. J. Harrison, and G. Beylkin, J. Phys.: Conf. Ser. **16**, 461 (2005).

[25] A. Bulgac and M. M. Forbes, arXiv:0808.1436.

[26] A. Bulgac and M. M. Forbes, Phys. Rev. Lett. **101**, 215301 (2008).

[27] G. Bertsch, J. Dobaczewski, W. Nazarewicz, and J. Pei, Phys. Rev. A **79**, 043602 (2009).

[28] J. C. Pei, J. Dukelsky, and W. Nazarewicz, Phys. Rev. A **82**, 021603 (2010).

[29] K. Bennaceur and J. Dobaczewski, Comput. Phys. Commun. **168**, 96 (2005).

[30] A. Bulgac and K. J. Roche, J. Phys.: Conf. Ser. **125**, 012064 (2008).

[31] G. I. Fann, J. Pei, R. J. Harrison, J. Jia, J. Hill, M. Ou, W. Nazarewicz, W. A. Shelton, and N. Schunck, J. Phys.: Conf. Ser. **180**, 012080 (2009).

[32] P. Fulde and R. A. Ferrell, Phys. Rev. **135**, A550 (1964).

[33] A. I. Larkin and Y. N. Ovchinnikov, Sov. Phys. JETP **20**, 762 (1965).

[34] A. Bulgac, Phys. Rev. A **76**, 040502 (2007).

[35] J. C. Pei, A. T. Kruppa, and W. Nazarewicz, Phys. Rev. C **84**, 024311 (2011).

[36] Y. Shi, C. L. Zhang, J. Dobaczewski, and W. Nazarewicz, Phys. Rev. C **88**, 034311 (2013).

[37] J. Bartel, P. Quentin, M. Brack, C. Guet, and H.-B. Håkansson, Nucl. Phys. A **386**, 79 (1982).

[38] P. J. Borycki, J. Dobaczewski, W. Nazarewicz, and M. V. Stoitsov, Phys. Rev. C **73**, 044319 (2006).

[39] J. Dobaczewski, W. Nazarewicz, and M. V. Stoitsov, Eur. Phys. J. A **15**, 21 (2002).

[40] A. Blazkiewicz, V. E. Oberacker, A. S. Umar, and M. Stoitsov, Phys. Rev. C **71**, 054321 (2005).

[41] W. Nazarewicz, M. Bender, S. Ćwiok, P. Heenen, A. Kruppa, P.-G. Reinhard, and T. Vertse, Nucl. Phys. A **701**, 165 (2002).

[42] J. Dechargé, J.-F. Berger, M. Girod, and K. Dietrich, Nucl. Phys. A **716**, 55 (2003).

[43] P. Jachimowicz, M. Kowal, and J. Skalski, Phys. Rev. C **83**, 054302 (2011).

[44] D. G. Ravenhall, C. J. Pethick, and J. R. Wilson, Phys. Rev. Lett. **50**, 2066 (1983).

[45] W. G. Newton and J. R. Stone, Phys. Rev. C **79**, 055801 (2009).

[46] C. O. Dorso, P. A. Giménez Molinelli, and J. A. López, Phys. Rev. C **86**, 055805 (2012).

[47] A. S. Schneider, C. J. Horowitz, J. Hughto, and D. K. Berry, Phys. Rev. C **88**, 065807 (2013).

[48] G. B. Partridge, W. Li, R. I. Kamar, Y.-A. Liao, and R. G. Hulet, Science **311**, 503 (2006).